InSAR-derived Crustal Deformation and Reverse Fault Motion of the 2017 Iran-Iraq Earthquake in the Northwestern Part of the Zagros Orogenic Belt

Tomokazu Kobayashi, Yu Morishita, Hiroshi Yarai and Satoshi Fujiwara

(Published online: 5 March 2018)

Abstract

An inland earthquake with a moment magnitude of 7.3 occurred in western Iran / eastern Iraq on November 12, 2017. Applying an interferometric SAR (InSAR) analysis using ALOS-2 SAR data to the earthquake, we detected the crustal deformation in the northwestern part of the Zagros orogenic belt. We successfully obtained quasi-up-down and quasi-east-west displacement components by combining two sets of InSAR data. The results show that uplift occurred in the western part of the source region with ~90 cm at most, while in the east subsidence occurred with ~30 cm at most. Most of the source region moved westward with ~50 cm at most. Our preferred fault model shows that the observations can be accounted for by a nearly pure reverse fault motion with a slight dextral motion on a low-angle fault plane dipping northeast.

1. Introduction

An earthquake with a moment magnitude (M_w) of 7.3 (U. S. Geological Survey (USGS), 2017) struck western Iran / eastern Iraq on November 12, 2017 (UTC). The epicenter of the main shock determined by USGS (2017) is shown by the red star in Fig. 1. In this region, the collision between the Arabian and Eurasian plates has resulted in the formation of the Zagros Mountains. The red line in Fig. 1 represents the boundary between the plates (Bird, 2003). The Arabian plate moves northward relative to the Eurasian plate at a speed of ~2 cm/year (Vernant et al., 2004; Madanipour et al. 2013). The direction of the plate movement is oblique against the plate boundary. Owing to the active collision, the source region is subjected to a NS-oriented convergent stress produced by the motion of the Arabian plate (Vernant et al., 2004), which culminates in large historical earthquakes (Fig. 1).

Satellite synthetic aperture radar (SAR) data can provide detailed and spatially comprehensive ground information, and an interferometric SAR (InSAR) enables ground deformation to be measured with high precision. It can provide valuable information on the spatial features of the fault rupture. The primary purpose of this paper is to quickly report on the first results of the InSAR-derived crustal deformation and a preliminary fault model.

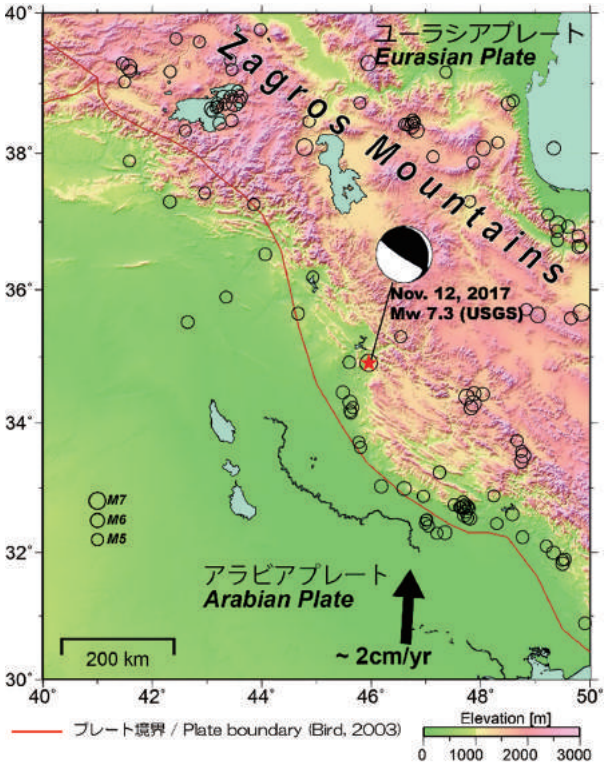

Fig. 1 Tectonic setting and topography map. The red star and beach ball stand for the epicenter location and the centroid-moment-tensor (CMT) solution, respectively (USGS, 2017). The red line indicates a plate boundary (Bird, 2003). The black arrow represents GPS-estimated movement of the Arabian plate relative to the Eurasian plate (Vernant et al., 2004; Madanipour et al. 2013). Open circles are historical earthquakes of M>5 and shallower than 50 km, listed in the USGS catalog.

2. SAR Data Analysis

A Japanese L-band synthetic aperture radar satellite, known as the Advanced Land Observing Satellite 2 (ALOS-2), made emergency observations for the purpose of detecting crustal deformation using InSAR. The images used in the study are listed in Table 1. We analyzed the ScanSAR-ScanSAR interferometry. The ScanSAR data we processed were produced by a full-aperture method in which range/azimuth compression was performed for the data whose gaps between neighboring bursts were filled with zeroes. The original interferograms were contaminated by a long-wavelength phase change noise of unknown causes, maybe due in part to the ionospheric effect. To pick out the crustal deformation only, we modeled the noises by estimating a phase curve with a second-order polynomial from far-field data, and subtracted the estimated phase curve from the original interferograms.

Table 1 Analyzed ALOS-2 images.

Observation Date	Aug. 09, 2016 Nov. 14, 2017	Oct. 04, 2017 Nov. 15, 2017
Flight Direction	Ascending	Descending
Beam Direction	Right	Right
Incidence Angle	47°	47°
Observation Mode	ScanSAR-ScanSAR	ScanSAR-ScanSAR
Perpendicular Baseline	-70 m	+160 m
Figure #	Fig. 2	Fig. 3

We processed the ALOS-2 data with GSISAR software (Fujiwara and Tobita, 1999; Tobita et al., 1999; Fujiwara et al., 1999; Tobita, 2003), and used ASTER GDEM for the InSAR analyses.

3. Ground displacement detected by InSAR

3.1 Line-of-sight component

Figs. 2a and 3a show interferograms obtained from ascending and descending orbit data, respectively. The coherence is high for the most part, probably due to the less-vegetated environment. An intensive deformation is located around 20 km NNW of Sarpol-e Zahab city. Two clear roundish fringes appear in both images. In Fig. 2a, slant range shortening signals are distributed in both lobes. The maximum line-of-sight (LOS) displacements are ~90 cm shortening for the southwestern lobe at most and ~15 cm shortening for the northeastern lobe at most. On the other hand, in Fig. 3a, slant range shortening and lengthening signals appear in the southwest and the northeast, respectively. The maximum LOS displacements are ~50 cm shortening for the southwestern lobe at most and ~35 cm lengthening for the northeastern lobe at most.

3.2 Quasi-up-down and quasi–east-west components

We have both descending and ascending data that are right-looking, in which the microwaves are emitted from two opposite directions—from the eastern sky and the western sky. This enables the derived LOS displacements to be converted into two components which are the quasi-up-down (QUD) and quasi-east-west (QEW) components (Fig. 4) (Fujiwara et al., 2000).

Figs 5a and 5b show the estimated QUD and QEW components, respectively. In Fig. 5a, the red and blue colors mean uplift and subsidence, respectively. We can identify a large uplift is distributed in the southwest of the epicenter with ~90 cm at most. In contrast, in and around the epicentral area, the ground has subsided with ~30 cm. In Fig. 5b, the red and green colors mean eastward and westward movements, respectively. There appear two main westward movement areas in the southwest with ~50 cm at most and in the northeast with ~35 cm at most. These spatial patterns are in agreement with crustal deformation produced by a reverse slip motion on a NW-SE striking fault plane.

3.3 Local Ground Displacement

Here we stress that we can identify many localized LOS displacements in the InSAR images, apart from the fault-slip-related crustal deformation. Figs. 2b and 2c show enlarged views of Fig. 2a. Note that we filtered out the long-wavelength signals corresponding to the fault-related deformation to pick out localized displacements. We can identify small and local but clear phase changes in the high-pass filtered image. Also, applying the high-pass

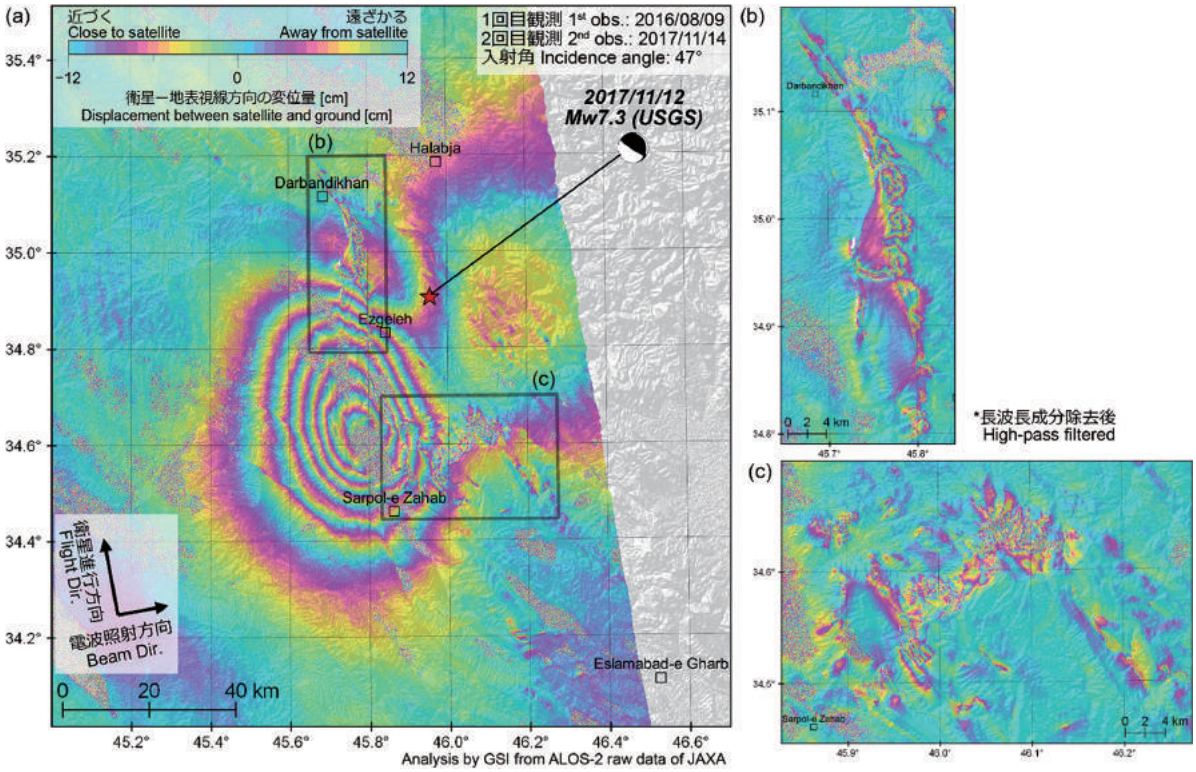

Fig. 2 An InSAR image for the ascending orbit. (a) An InSAR image covering the source region. (b) and (c) Enlarged views. A high-pass filter was applied to remove the long-wavelength signals.

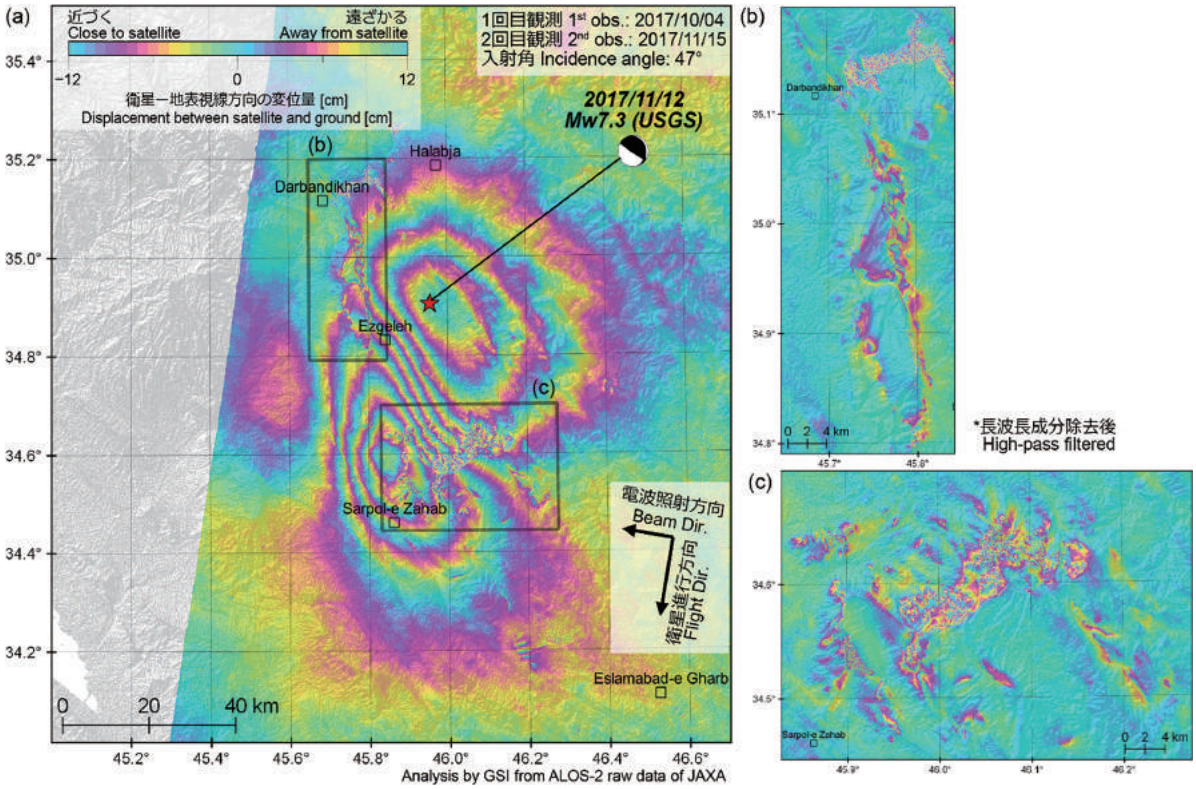

Fig. 3 Same as Fig. 2 but for the descending orbit data.

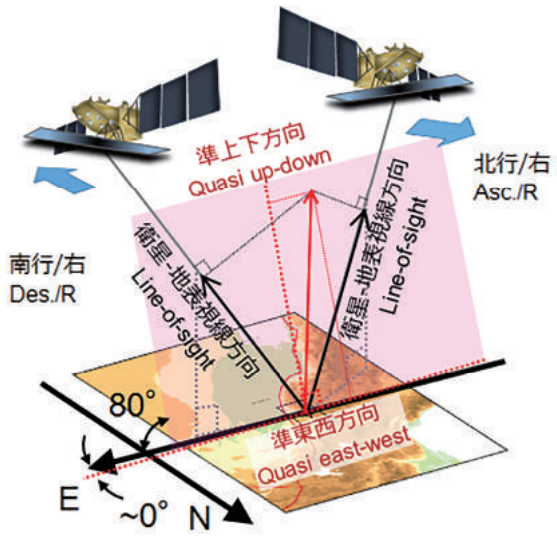

Fig. 4 Geometry of 2.5D displacement analysis.

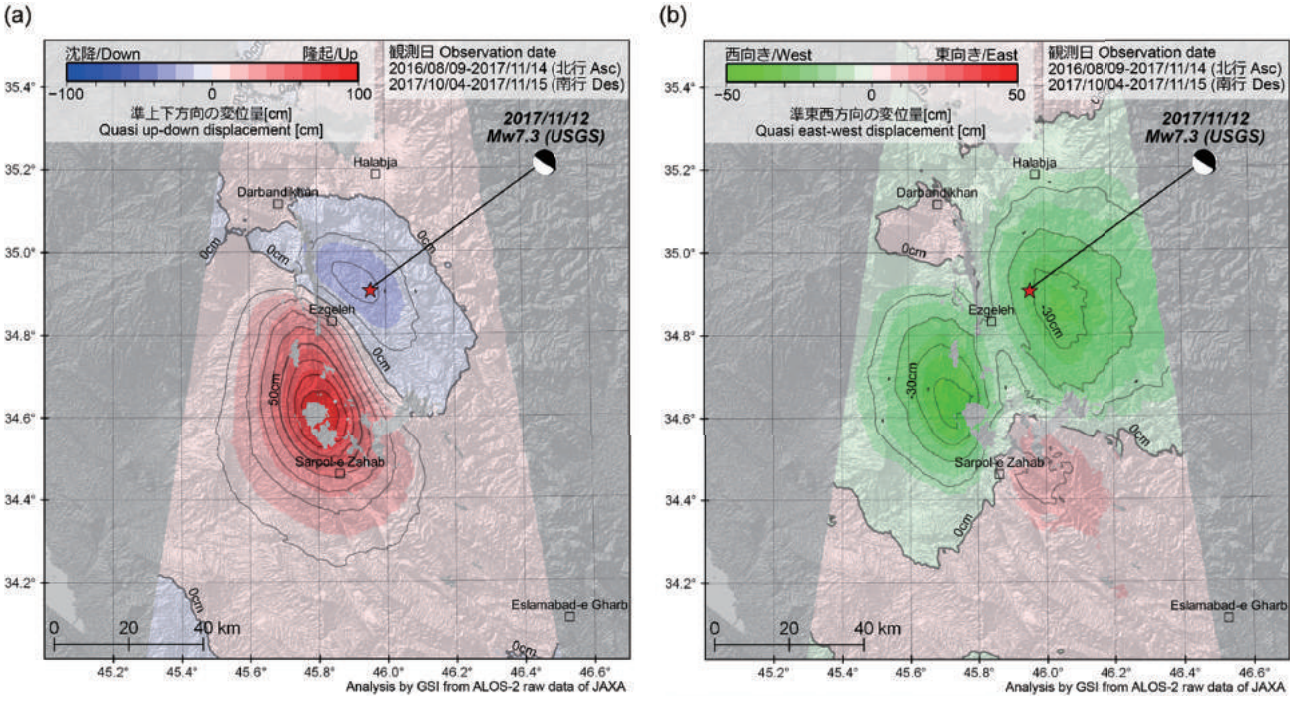

Fig. 5 2.5D displacement fields. (a) A quasi-up-down component. The red and blue colors mean uplift and subsidence, respectively. (b) A quasi-east-west component. The red and green colors mean eastward and westward movements, respectively.

filter to the InSAR data of descending orbit in the same manner, the localized phase changes can be identified at almost the same locations, but with the opposite sign, indicating that the horizontal (EW) displacement is dominant (Figs. 3b and 3c). Most of the localized displacements are detected at mountain slopes and are consistent with downward movement along the slopes. These displacements might have been triggered by the seismic motion.

3.4 Linear Surface Ruptures

The InSAR images generally show elastic deformation caused by the main earthquakes, but many other linear discontinuities showing displacement are also

found (Fujiwara et al., 2016). We mapped the ruptures in the two InSAR images in Fig. 6. Most of the ruptures are likely secondary faults that are not directly related to the main earthquake but whose slip was probably triggered by the main earthquake or aftershocks.

4. Fault model

We constructed a slip distribution model by a least squares approach (e.g., Kobayashi et al. 2015). In the inversion, we used both the ascending and the descending orbit data shown in Figs. 2a and 3a. The fault geometry was assumed to be a plane fault. We set a rectangular fault of 100 km long and 80 km wide, and the fault was divided into square patches of 5 × 5 km in size. The fault geometry basically followed the USGS's Centroid Moment Tensor (CMT) solution (USGS, 2017). According to previous geological and seismological studies, a low-angle thrust system with a NE-dipping plane may have developed in this region (e.g., Vergés et al., 2011; Madanipour et al. 2013). Thus we followed this idea; that is, we took a nodal plane dipping to NE with a dip angle of 16°. The strike was fixed so as to be almost parallel to the plate boundary (Bird, 2003). We adjusted the fault depth so that the USGS's hypocenter (19 km in depth) could be on the fault plane. Consequently, the fault top position was fixed to a depth of 3 km below the surface.

We used the dislocation equations proposed by Okada (1985) to calculate the surface displacement in the LOS directions. Only the dip-slip and strike-slip components were estimated for each patch. A large number of model parameters often give rise to instability of the solution. To stabilize the solution, we imposed a spatial smoothness constraint on the slip distribution using a Laplacian operator. The relative weight of the constraints was determined by Akaike's Baysian information criterion (Akaike, 1980). Here, we assumed a rigidity of 30 GPa.

The data points of the interferograms were too many to be easily assimilated in a modeling scheme. In order to reduce the number of data for the modeling analysis, we resampled the interferogram data beforehand, using a quadtree decomposition method. Essentially, we followed an algorithm presented by Jónsson et al. (2002). For a given quadrant, after removing the mean, if the residue was greater than a prescribed threshold (5 cm in our case), the quadrant was further divided into four new quadrants. This process was iterated either until each block met the specified criterion or until the quadrant reached a minimum block size (8 × 8 pixels in our case). Upon application of this procedure, the sizes of the respective interferogram data sets were reduced from 1,443,200 to 239 for the ascending data and to 279 for the descending data.

Fig. 7 shows the estimated slip distribution, and Figs. 8 and 9 show the LOS displacements calculated from the derived model and the residuals, respectively. Our model reproduces well the LOS displacement fields for both the ascending and descending data. Fig. 10 shows the model-predicted UD, EW, and NS displacement components. Both UD and EW displacement fields are reproduced well.

A major slip with a maximum slip amount of approximately 3 m occurred beneath the southeastern part of the epicenter. The slips were a nearly pure reverse fault motion, but with a slight right-lateral motion. The obtained oblique slip was consistent with the tectonic background that the Arabian plates obliquely subside against the Eurasian plate (Fig. 1). The moment is estimated to be 1.18×10^{20} Nm, equivalent to M_w 7.31. This is consistent with the seismic moment determined with seismic data (USGS CMT: 1.12×10^{20} Nm (M_w 7.3); Global CMT Catalog (2017): 1.72×10^{20} Nm (M_w 7.4)).

5. Concluding remarks

We conducted InSAR analysis using ALOS-2 data to detect the crustal deformation associated with the 2017 Iran-Iraq earthquake. The following conclusions were obtained from the analyses:

1. Large displacement (~90 cm upward and ~50 cm westward) was detected around 20 km NNW of Sarpol-e Zahab.
2. Around the epicenter, ~30 cm downward and ~35 cm westward displacement was detected.
3. Apart from the deformation associated with the fault slip, lots of localized displacements were detected at mountain slopes, and might have been triggered by the seismic motion.

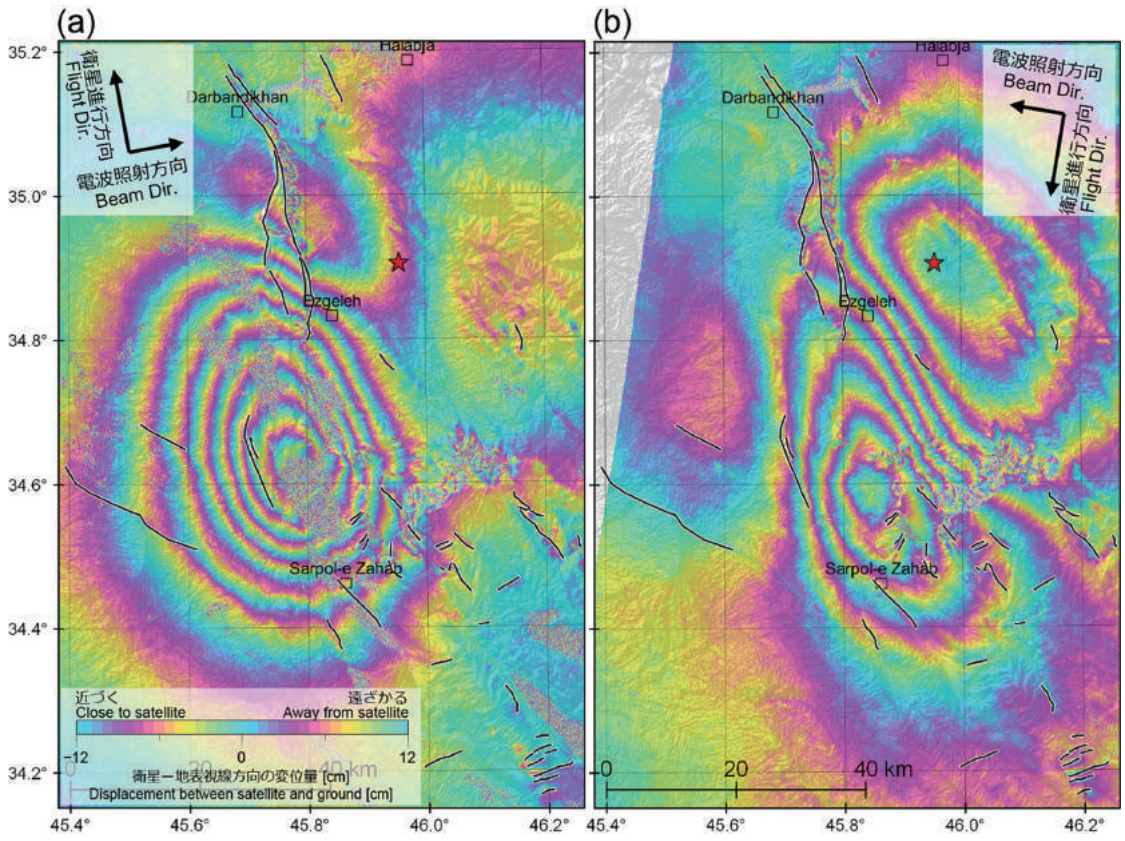

Fig. 6 InSAR images for the ascending orbit (a) and the descending orbit (b). The solid lines show the identified linear surface ruptures.

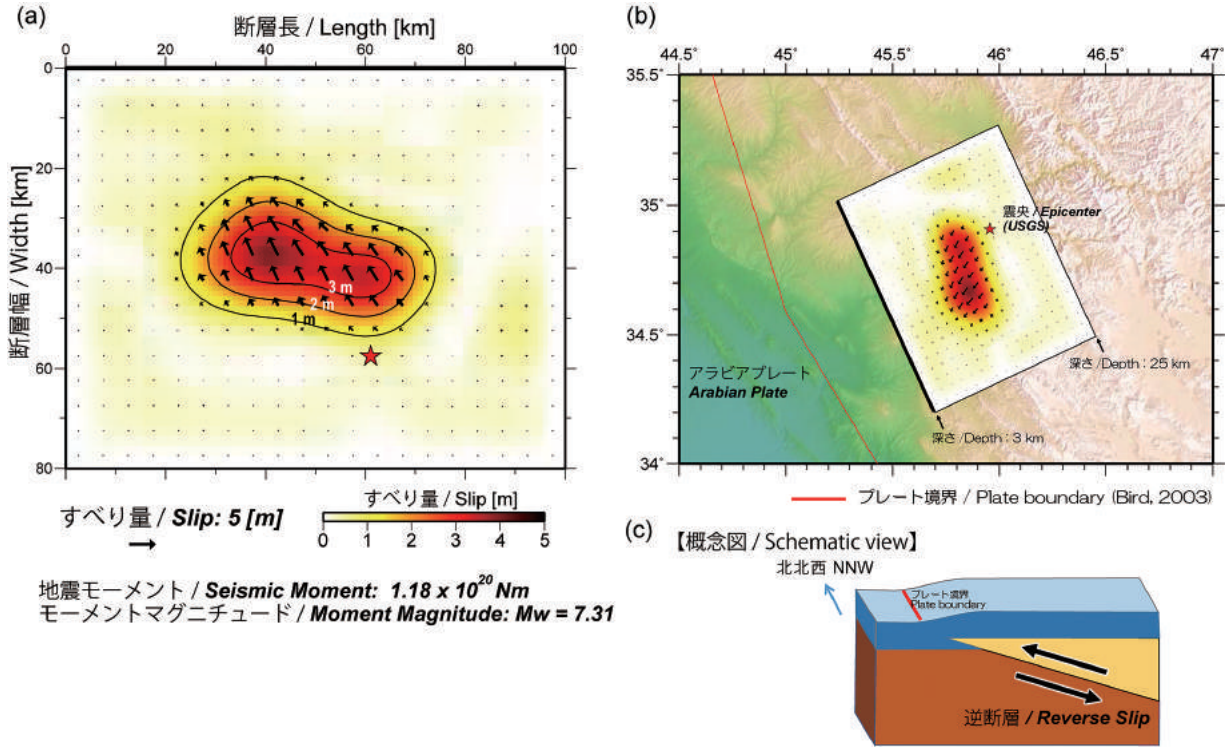

Fig. 7 (a) Slip distribution model. The arrows show slip vectors of the hanging wall. The contour interval is 1 m. The red star represents the hypocenter projected on the fault plane. (b) Slip distribution on map. (c) Schematic view of the source mechanism.

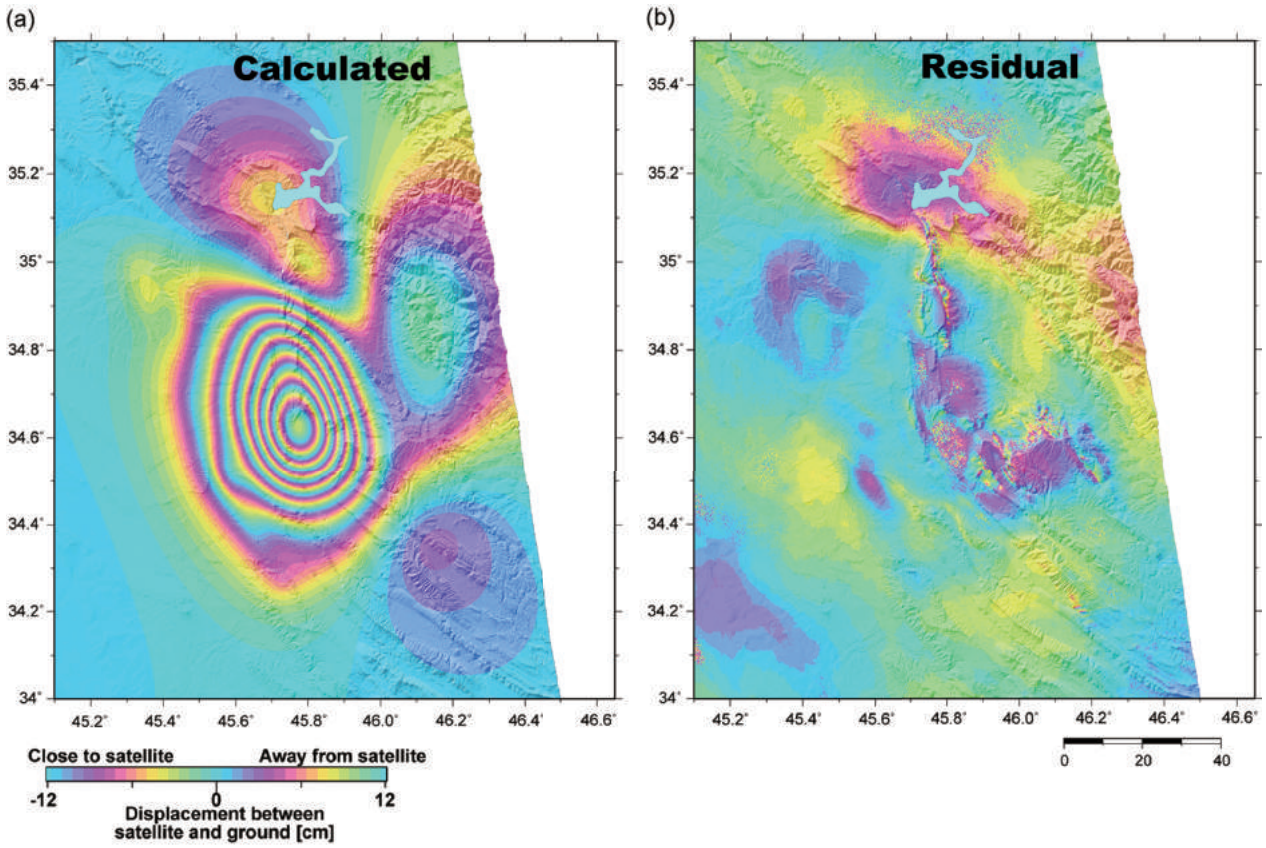

Fig. 8 (a) Model-calculated LOS displacement for the ascending orbit data. (b) Residual.

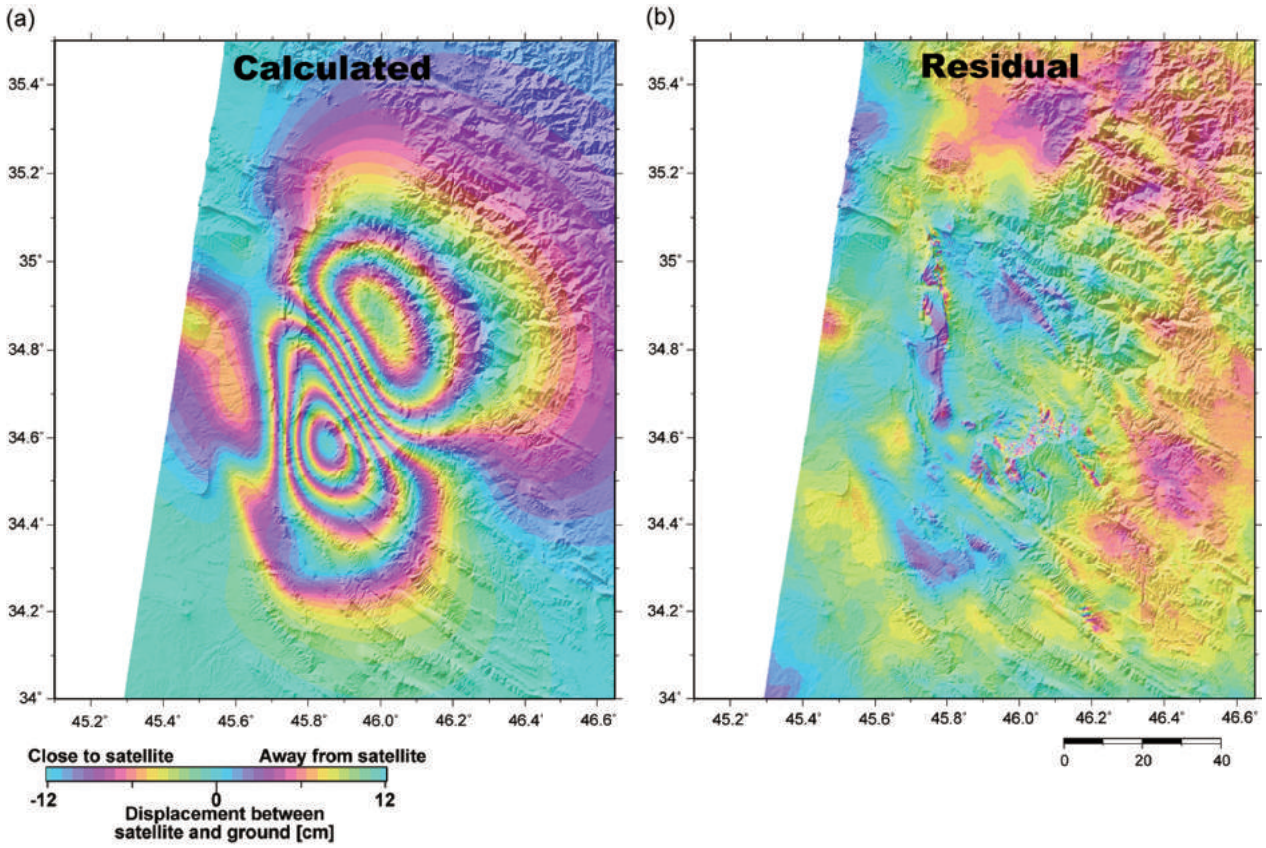

Fig. 9 (a) Same as Fig. 7 but for the descending orbit data.

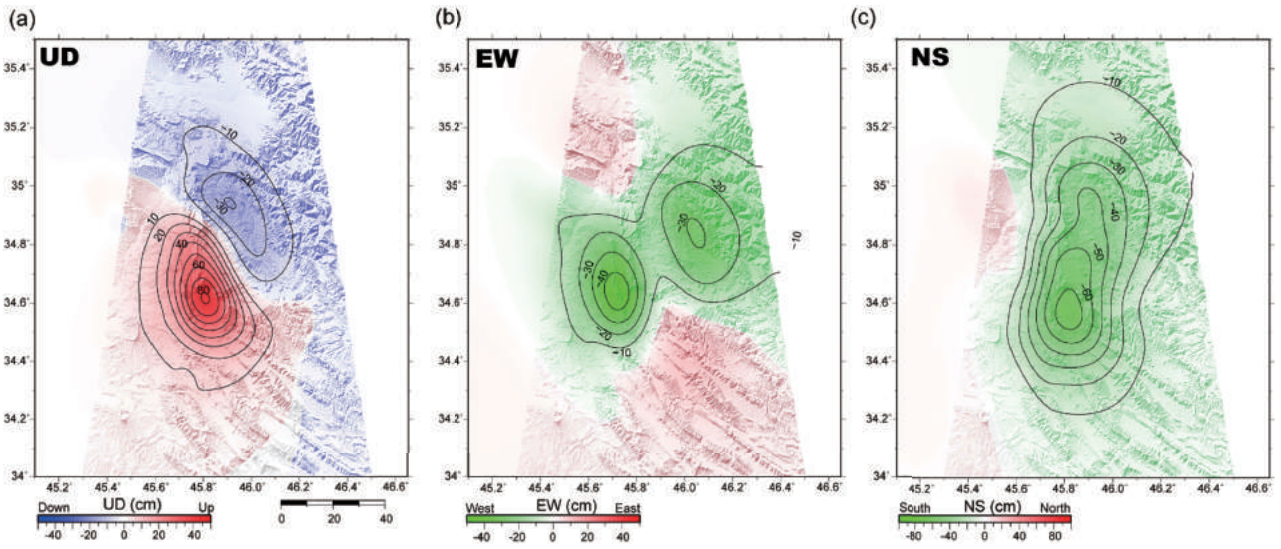

Fig. 10 Model-predicted displacements. (a) Up-Down component. (b) East-West component. (c) North-South component.

4. Our fault model shows a nearly pure reverse-fault with a slight dextral slip motion. A major slip occurred with a slip amount of ~3 m beneath the southwestern part of the epicenter.
5. The estimated moment magnitude was 7.31 (seismic moment 1.18×10^{20} Nm).

Acknowledgments

ALOS-2 data were provided by the Earthquake Working Group under a cooperative research contract with the Japan Aerospace Exploration Agency (JAXA). The ownership of ALOS-2 data belong to JAXA. We used Generic Mapping Tools (GMT) provided by Wessel and Smith (1998) to construct the figures for the fault model. We used ASTER GDEM for the InSAR analyses. ASTER GDEM is a product of the National Aeronautics and Space Administration (NASA) and the Ministry of Economy, Trade and Industry (METI).

References

Akaike, H (1980): Likelihood and the Bayes procedure. In: Bernardo. JM, DeGroot. MH, Lindley. DV, Smith. AFM, (eds) Bayesian Statistics. University Press, Valencia.

Bird, P. (2003): An updated digital model of plate boundaries, Geochemistry Geophysics Geosystems, 4(3), 1027.

Fujiwara, S and M. Tobita (1999): SAR interferometry techniques for precise surface change detection, J. Geod. Soc. Japan, 45, 283-295 (in Japanese with English abstract).

Fujiwara, S., M. Tobita, M. Murakami, H. Nakagawa and P. A. Rosen (1999): Baseline determination and correction of atmospheric delay induced by topography of SAR interferometry for precise surface change detection, J. Geod. Soc. Japan, 45, 315-325 (in Japanese with English abstract).

Fujiwara, S., T. Nishimura, M. Murakami, H. Nakagawa, M. Tobita and P. A. Rosen (2000): 2.5-D surface deformation of a M6.1 earthquake near Mt Iwate detected by SAR interferometry, Geophys. Res. Lett., 27, 2049-2052.

Fujiwara, S., H. Yarai, T. Kobayashi, Y. Morishita, T. Nakano, B. Miyahara, H. Nakai, Y. Miura, H. Ueshiba, Y. Kakiage and H. Une (2016): Small-displacement linear surface ruptures of the 2016 Kumamoto earthquake sequence detected by ALOS-2 SAR interferometry, Earth Planets Space, 68: 160.

Global Centroid Moment Tensor Catalog (2017): 201711121818A IRAN-IRAQ BORDER REGION,

http://www.globalcmt.org (accessed Dec.7, 2017).

Jónsson, S., H. Zebker, P. Segall and F. Amelung (2002) : Fault slip distribution of the 1999 Mw 7.1 Hector Mine, California, earthquake, estimated from satellite radar and GPS measurements, Bull. Seism. Soc. Amer., 92, 1377-1389.

Kobayashi, T., Y. Morishita and H. Yarai (2015): Detailed crustal deformation and fault rupture of the 2015 Gorkha earthquake, Nepal, revealed from ScanSAR-based interferograms of ALOS-2, Earth Planets Space, 67:201.

Madanipour, S., Ehlers, T., Yassaghi, A., Rezaeian, M., Enkelmann E and Bahroudi, A (2013): Synchronous deformation on orogenic plateau margins: Insights from the Arabia–Eurasia collision, Tectonophysics, 608, 440-451.

http://dx.doi.org/10.1016/j.tecto.2013.09.003 (accessed Dec.7, 2017).

Okada, Y (1985): Surface deformation due to shear and tensile faults in a halfspace, Bull Seismol Soc Am, 75, 1135-1154.

Tobita, M., S. Fujiwara, M. Murakami, H. Nakagawa and P. A. Rosen (1999): Accurate offset estimation between two SLC images for SAR interferometry, J. Geod. Soc. Japan, 45, 297-314 (in Japanese with English abstract).

Tobita, M (2003): Development of SAR interferometry analysis and its application to crustal deformation study, J. Geod. Soc. Japan, 49, 1-23 (in Japanese with English abstract).

U. S. Geological Survey (2017): M7.3 – 30km S of Halabjar, Iraq. https://earthquake.usgs.gov/earthquakes/eventpage/us2000bmcg#executive (accessed Dec.7, 2017).

Vergés, J., Saura, E., Casciello, E., Fernàndez, M., Villaseñor, A., Jiménez-Munt, I., García-Castellanos, D (2011): Crustal-scale cross-sections across the NW Zagros belt: implications for the Arabian margin reconstruction, Geological Magazine, 148, 739-761.

Vernant, Ph., F. Nilforoushan, D. Hatzfeld, M.R. Abbassi, C. Vigny, F. Masson, H. Nankali, J. Martinod, M. Ghafory-Ashtiany, R. Bayer, F. Tavakoli and J. Chéry (2004) : Present-Day Crustal Deformation and Plate Kinematics in the Middle East Constrained by GPS Measurements in Iran and Northern Oman, Geophys. J., Int., 157, 381-398.

Wessel, P and Smith, WH (1998): New, improved version of Generic Mapping Tools released, Eos Trans AGU, 79, 579.